

Physics-informed neural networks for phase-field simulation in designing high energy storage performance polymer nanocomposites

Cite as: Appl. Phys. Lett. **126**, 052901 (2025); doi: [10.1063/5.0244002](https://doi.org/10.1063/5.0244002)

Submitted: 15 October 2024 · Accepted: 18 January 2025 ·

Published Online: 5 February 2025



Dong-Duan Liu,¹  Qiao Li,^{1,a)}  Yu-Jie Zhu,²  Ruo-Jie Cheng,¹ Tan Zeng,¹ Hongxiao Yang,¹ Jun Ma,³ 
Jin-Liang He,⁴  Qi Li,⁴  and Chao Yuan^{1,a)} 

AFFILIATIONS

¹College of Electrical and Information Engineering, Hunan University, Changsha 410082, China

²Department of Materials Science and Engineering, University of Wisconsin-Madison, Madison, Wisconsin, 53706, USA

³School of Electrical, Electronic and Mechanical Engineering, University of Bristol, Bristol 27267, United Kingdom

⁴State Key Laboratory of Power System, Department of Electrical Engineering, Tsinghua University, Beijing 100084, China

^{a)}Authors to whom correspondence should be addressed: qiaoli@hnu.edu.cn and chaoyy@outlook.com

ABSTRACT

Dielectric polymers for electrostatic energy storage are used in modern electronic and electrical systems, and their performance can be significantly enhanced through doping with ultralow content nanofillers to improve energy storage performance. Understanding the underlying physical mechanisms of polymer nanocomposites is essential for designing high-performance dielectric polymers. This paper presents a conduction model that integrates Richardson-Schottky emission and hopping conduction to describe charge injection and transport in polymer composites. Phase-field simulations, incorporating electrical, thermal, and mechanical breakdown mechanisms, investigate the influence of nanofiller volume fraction, size, and dielectric constant on the dielectric response and breakdown behaviors under high temperature and electric fields. We propose the Physics-Informed Neural Networks for phase-field simulation that integrates the physical rules of charge transport, phase evolution, and boundary conditions. By embedding phase field models within the Physics-Informed Neural Networks' structure, this method demonstrates the ability to predict the breakdown strength and energy density of polymer nanocomposites. This work provides crucial guidelines for designing high-performance dielectric energy storage capacitors under extreme conditions.

Published under an exclusive license by AIP Publishing. <https://doi.org/10.1063/5.0244002>

Dielectric polymers are extensively used in high-performance applications such as energy storage, pulse power systems, and electronic devices.^{1–4} Biaxially oriented polypropylene (BOPP) is currently the dielectric material of choice for the manufacture of commercial capacitors due to its inherent advantages, including lightweight, high breakdown strength, and low energy loss.^{5,6} The relative dielectric constant and breakdown strength are essential in designing high-discharged energy density (U_e) dielectric polymer with low loss.^{7–9} The U_e is governed by two important factors of electric displacement and E , as presented in Fig. S1. Thus, the key figure of merit for designing high-discharged energy density capacitors is to increase the relative dielectric constant while increasing the breakdown strength.^{10,11} Researchers have explored synthesizing high energy storage performance dielectric polymer composites by introducing inorganic fillers with high dielectric constant or organic semiconductors with strong electron affinity.^{12–16} However, Incorporating high dielectric constant

fillers can effectively increase the relative dielectric constant of polymers but reduces their breakdown strength.^{3,16} Introducing organic semiconductors with strong electron affinity improves breakdown strength without significantly enhancing the dielectric properties of the polymers.^{14,15}

To obtain the trade-off of the dielectric constant and breakdown strength, nanostructure engineering has been proposed to develop high-performance dielectric polymers.⁹ It has been found that the dielectric constant of composites doped with trace nanofillers with a similar dielectric constant to the polymer matrix can be significantly improved by nanostructure engineering of nanofillers.^{9,13} However, the impact of nanostructure interface configurations and distributions on the macroscopic energy storage performance of dielectric polymers remains poorly understood.¹⁷ Therefore, a comprehensive investigation of the underlying structure–property relationship between interfacial conformation and polarization behavior can drive the innovative

design of nanostructured engineering and lead to the development of high-discharge density dielectric materials.^{9,13,17} Incorporating nanofillers into polymer matrixes can improve material properties, predicting the behavior and interaction between the fillers and the polymer remains challenging.^{9,18,19} Phase field simulations offer a robust method to simulate the evolution of microstructures in these systems under complex physical fields.^{20–22} Besides, Physics-Informed Neural Networks (PINNs) provide a promising solution by embedding physical rules directly into neural networks to reduce computational costs while maintaining accuracy.^{23–25} PINNs can effectively learn complex interactions in polymer nanocomposites, governed by the physical mechanisms in the breakdown evolution process.^{26–28}

In this work, we employ the phase field simulations with the electrical-thermal-mechanical breakdown mechanism to investigate the influences of volume fraction, size, and dielectric constant of fillers on dielectric response and breakdown behaviors. Electrical field distribution, phase evolution, electrical, thermal, and strain energy density were conducted to clarify the underlying physical mechanisms of dielectric response and breakdown with different volume fractions, sizes, and dielectric constants of fillers. Additionally, we propose the PINNs integrated with various conduction models, phase evolution, and boundary conditions to perform the phase breakdown process of composites. By integrating phase field models into the PINN framework, PINNs provide a robust tool for designing advanced polymer nanocomposites with optimized performance. All simulation details are presented in the [supplementary material](#).

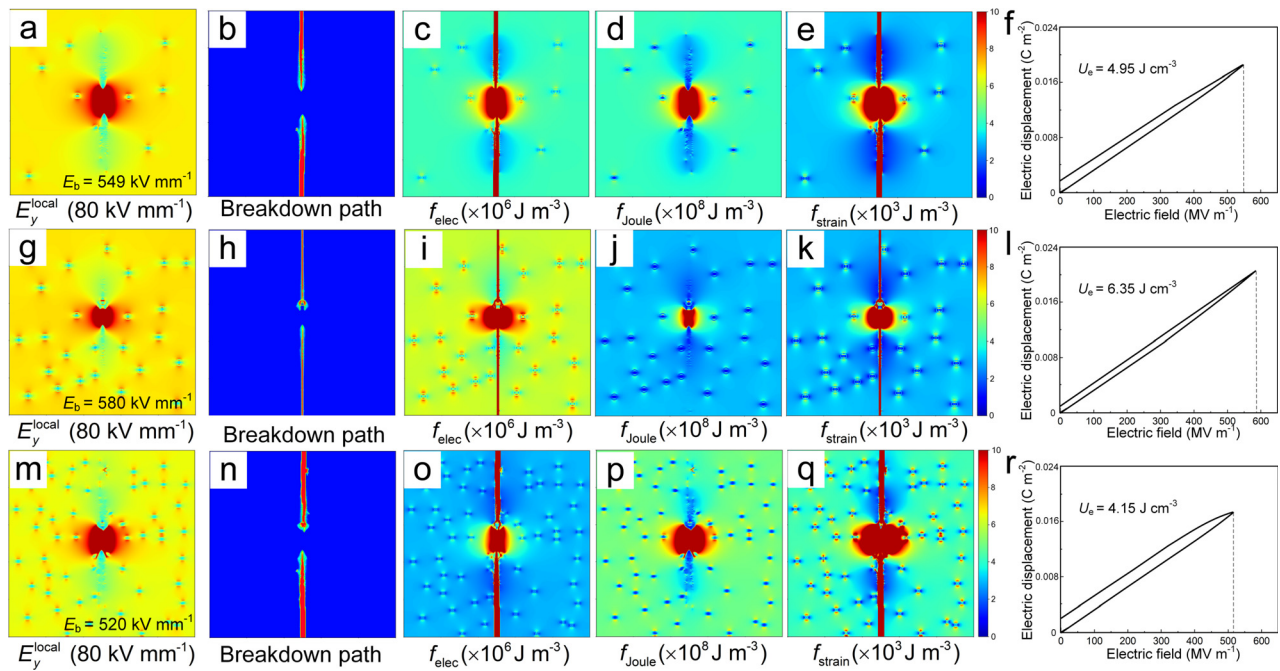
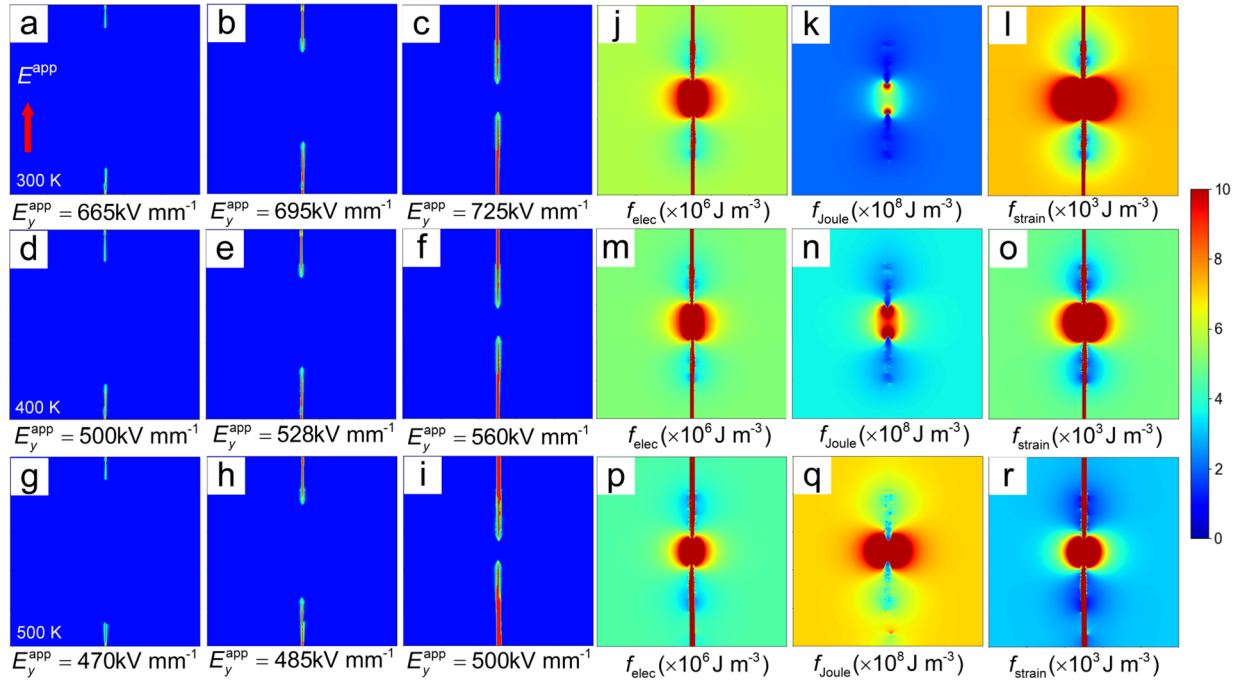
We perform phase field simulations to stimulate breakdown evolution under different applied electric fields and temperatures. Considering the bipolar charge injection behavior, the initial breakdown phase is propagated from the two needle electrodes. The breakdown evolution states of the breakdown process at 300, 400, and 500 K are presented in [Figs. 1\(a\)–1\(i\)](#), respectively. At 300 K, the breakdown phase begins at 665 kV mm^{-1} and breaks down at 725 kV mm^{-1} , as shown in [Figs. 1\(a\)–1\(c\)](#). As temperature increases to 400 K, the electric field threshold decreases to 500 kV mm^{-1} and the polymer is almost completely broken down at 560 kV mm^{-1} . At 500 K, the threshold decreases to 470 kV mm^{-1} with breakdown occurring at 500 kV mm^{-1} . Therefore, the breakdown strength decreases by 225 kV mm^{-1} from 725 to 500 kV mm^{-1} for a dramatic temperature increase in 200 K from 300 to 500 K. This decrease is attributed to increased electron injection and thermal excitation, leading to greater conduction losses and reduced breakdown strength.¹⁴

[Figures 1\(j\)–1\(r\)](#) show the energy density of electric, Joule heat, and strain at the forefront and along the breakdown path are considerably higher than in surrounding regions, thus driving the prolongation of the breakdown path. Since the dielectric constant of polymers is insensitive to temperature, the electric energy density mainly arises from the different magnitudes of the electric field. According to $U_e = 1/2 \epsilon_0 \epsilon_r E^2$, the electric energy density decreases slightly from 300 to 500 K, due to the decrease in breakdown strength with increasing temperature. The electrical conductivity of PI varies by several orders of magnitude from $\sim 10^{-15} \text{ S m}^{-1}$ at 300 K to $\sim 10^{-12} \text{ S m}^{-1}$ at 500 K. At 500 K, the breakdown strength is 500 kV mm^{-1} , which is only 68% of that at 300 K, which is 725 kV mm^{-1} . The Joule energy density depends on the electrical conductivity and applied electric field. Hence, the Joule energy density is completely different under different temperatures, as shown in [Figs.](#)

[1\(k\)](#), [1\(n\)](#), and [1\(q\)](#). As presented in [Figs. 1\(l\)](#), [1\(o\)](#), and [1\(r\)](#), the strain energy density distributions are different. The strain energy density $\sim 7.29 \times 10^3 \text{ J m}^{-3}$ was calculated with an applied electric field of 725 kV mm^{-1} and Young's modulus of 3.8 GPa at 300 K. As the temperature rises, the thermal movement of the polymer chains is intense, resulting in a decrease in Young's modulus and breakdown strength. The strain energy density $\sim 2.85 \times 10^3 \text{ J m}^{-3}$ was calculated with an applied electric field of 500 kV mm^{-1} and Young's modulus of 2.2 GPa at 500 K. As a result, the strain energy densities are slightly different, although the breakdown strength and Young's modulus change significantly at different temperatures.

First, we established three models of PI/0.1 vol.% Al_2O_3 , PI/0.3 vol.% Al_2O_3 , and PI/1 vol.% Al_2O_3 to study the volume fraction effect of nanofillers on energy storage performance by phase-field simulations. The diameter of nanofiller Al_2O_3 and temperature were set to 5 nm and 473 K, respectively. [Figures 2\(a\)](#), [2\(g\)](#), and [2\(m\)](#) present the electric field distribution of ultralow content 0.1 vol.% Al_2O_3 , moderate content 0.3 vol.% Al_2O_3 , and high content 1 vol.% Al_2O_3 PI-based nanocomposites, respectively. The breakdown strength of PI/0.1 vol.% Al_2O_3 is 549 kV mm^{-1} . If the doping concentration of Al_2O_3 is increased to 0.3 vol.%, the breakdown strength increases to 580 kV mm^{-1} , and when the content of Al_2O_3 is further increased to 1 vol.%, the breakdown strength decreases to 520 kV mm^{-1} . The dielectric constants of the composites were calculated through numerical solutions of the electrostatic equilibrium equation, yielding values of 3.7, 4.3, and 3.46 for PI/0.1 vol.%, PI/0.3 vol.%, and PI/1 vol.% Al_2O_3 , and the breakdown dynamic evolution is presented in [Figs. 2\(b\)](#), [2\(h\)](#), and [2\(n\)](#), respectively. As shown in [Figs. 2\(c\)](#), [2\(i\)](#), and [2\(o\)](#), the variation in electric energy density is mainly attributable to the different magnitudes of the electric field and the dielectric constants. The Joule heat energy density indicates the heat distribution inside nanocomposites, reducing the electrical conductivity of nanocomposites can inhibit the thermal breakdown and improve the breakdown strength at high temperatures and high fields. [Figures 2\(d\)](#), [2\(j\)](#), and [2\(p\)](#) present the Joule heat energy density under the doping volume fraction of Al_2O_3 0.1 vol.%, 0.3 and 1 vol.%, respectively. The results demonstrate that PI/0.3 vol.% Al_2O_3 achieves the lowest electrical conductivity, effectively trapping free charges and improving breakdown strength under high temperatures and electric fields. Additionally, strain energy density was analyzed, showing that PI/0.3 vol.% Al_2O_3 exhibits the lowest strain energy, indicating moderate concentration can enhance mechanical strength due to Al_2O_3 with high Young's modulus, as shown in [Figs. 2\(e\)](#), [2\(k\)](#), and [2\(q\)](#). The electric displacement (D)–electric field (E) loop of PI/different volume fractions of Al_2O_3 was constructed to evaluate the energy storage performance, as shown in [Figs. 2\(f\)](#), [2\(l\)](#), and [2\(r\)](#), respectively. The phase field simulation results show PI/0.3 vol.% Al_2O_3 nanocomposites can obtain the highest energy storage density of 6.35 J cm^{-3} . High energy storage density is attributed to the highest dielectric response and breakdown strength of Al_2O_3 with suitable doping content. Hence, doping with appropriate nanofillers is crucial in designing high energy storage performance polymer nanocomposites.^{9,22,29}

The size effect of Al_2O_3 on the energy storage performance was further investigated based on the simulation results of the volume fraction effect of PI/ Al_2O_3 nanocomposite. We develop three sizes of Al_2O_3 with 5, 10, and 20 nm to perform the phase-field simulations at a fixed volume fraction of 0.3 vol.% Al_2O_3 . As the nanofiller size



increased, the dielectric response weakened due to interfacial region overlap, as illustrated in Fig. S5. Quantum size effect shows that the bandgap of Al_2O_3 decreases from 9.7 eV (5 nm) to 6.3 eV (20 nm), size reduction significantly increases the surface atom ratio, introducing more deep traps in the nanocomposites to inhibit charge transport.³⁰ Figures 3(a), 3(f), and 3(k) present the electric field distribution and breakdown evolution of PI/0.3 vol.% Al_2O_3 (5 nm), PI/0.3 vol.% Al_2O_3 (10 nm), and PI/0.3 vol.% Al_2O_3 (20 nm), respectively. The breakdown strengths for PI/0.3 vol.% Al_2O_3 nanocomposites were 580, 538, and 520 kV mm^{-1} for 5, 10, and 20 nm Al_2O_3 , respectively, indicating that smaller nanoparticles improved breakdown strength. Dielectric constants were calculated as 4.3, 3.93, and 3.56 for the respective sizes by performing the phase field simulations. As shown in Figs. 3(b), 3(g), and 3(l), the electric energy density of PI/ Al_2O_3 nanocomposites with different sizes demonstrates that doping with ultralow volume fraction of small-sized nanoparticles can simultaneously improve the dielectric constant and breakdown strength. The Joule heat energy density of PI/0.3 vol.% Al_2O_3 (5 nm), PI/0.3 vol.% Al_2O_3 (10 nm), and PI/0.3 vol.% Al_2O_3 (20 nm) nanocomposites is presented in Figs. 3(c), 3(h), and 3(m), respectively. The PI/0.3 vol.% Al_2O_3 (5 nm) nanocomposites indicate the lowest Joule heat energy density among the three polymer nanocomposites. The lowest electrical conductivity of PI/0.3 vol.% Al_2O_3 (5 nm) nanocomposites is attributed to the wide bandgap and the deep traps introduced by surface defect states of Al_2O_3 (5 nm). Furthermore, the strain energy density of the three

nanocomposites decreased slightly from $\sim 3.7 \times 10^3 \text{ J m}^{-3}$ of PI/0.3 vol.% Al_2O_3 (5 nm) to $\sim 3 \times 10^3 \text{ J m}^{-3}$ of PI/0.3 vol.% Al_2O_3 (20 nm), as presented in Figs. 3(d), 3(i), and 3(n). The D - E loops show the discharge energy density gradually decreases while the diameter of nanofillers increases, as demonstrated in Figs. 3(e), 3(j), and 3(o). Above the analysis of size effect on energy storage density, doping with small-sized nanofillers can effectively reduce the carrier mobility and suppress the conduction loss, thereby improving the breakdown strength and dielectric constant of nanocomposites.^{29,31,32}

As mentioned above, the volume fraction and size of Al_2O_3 in polymer nanocomposites effectively modulate energy storage performance by influencing the dielectric response and quantum size effects.⁹ To further investigate the impact of different nanofillers, phase field simulations were conducted with fixed volume fractions (0.3 vol.%) and sizes (5 nm) for SiO_2 , MgO , and Al_2O_3 . The electrical distribution and breakdown strengths of PI/0.3 vol.% SiO_2 , PI/0.3 vol.% MgO , and PI/0.3 vol.% Al_2O_3 are presented in Figs. 4(a), 4(f), and 4(k), respectively. The electric field distribution reveals significant differences in breakdown strengths, with PI/0.3 vol.% MgO reaching the highest breakdown strength of 600 kV mm^{-1} , demonstrating its superior dielectric robustness. The dielectric constants were calculated as 4.05, 4.1, and 4.3 for the PI/ SiO_2 , PI/ MgO , and PI/ Al_2O_3 nanocomposites, respectively, showing that electric density distribution is primarily determined by electric field strengths, as shown in Figs. 4(b), 4(g), and 4(l). The dielectric response results illustrate that the improved

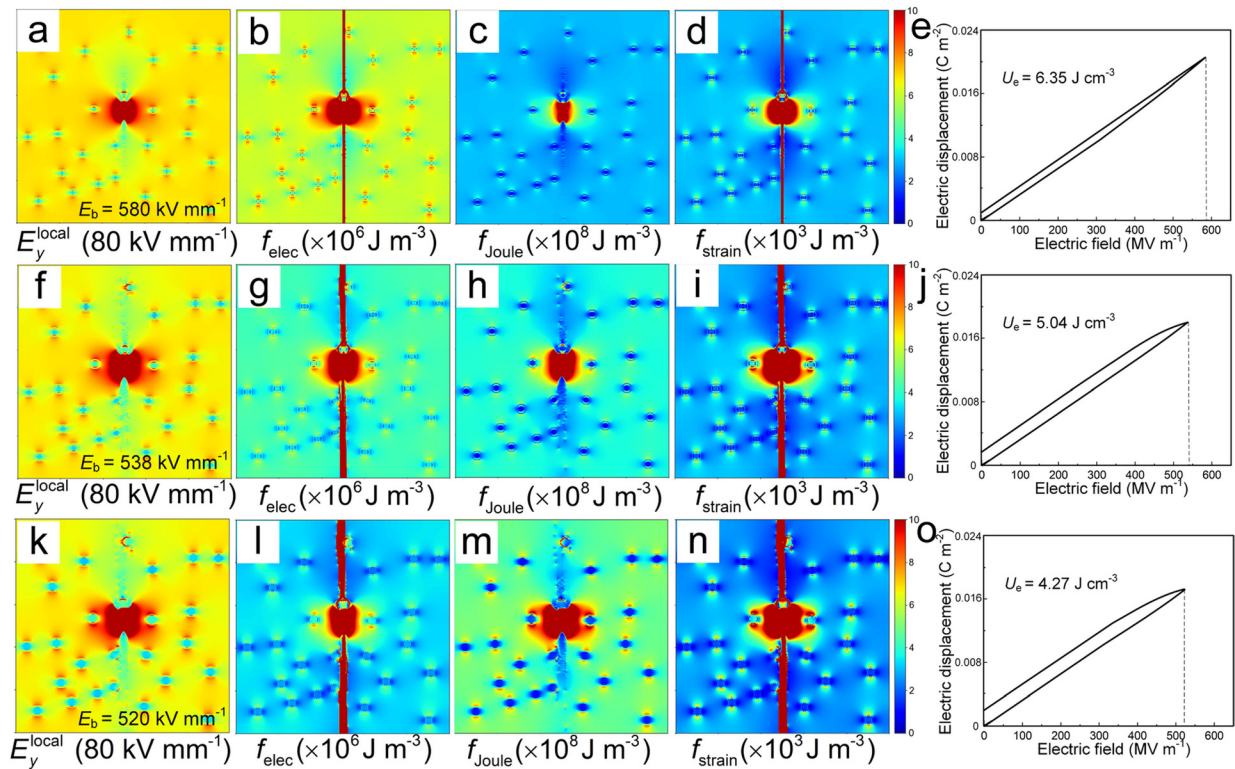


FIG. 3. Size effect on energy storage performances of PI/0.3 vol.% Al_2O_3 nanocomposites. Electrical field distribution, electric energy density f_{elec} , Joule heat energy density f_{Joule} , strain energy density f_{strain} , and calculated D - E loop of nanocomposites with nanofillers of different sizes. (a)–(e) Al_2O_3 (5 nm), (f)–(j) Al_2O_3 (10 nm), and (k)–(o) Al_2O_3 (20 nm), respectively.

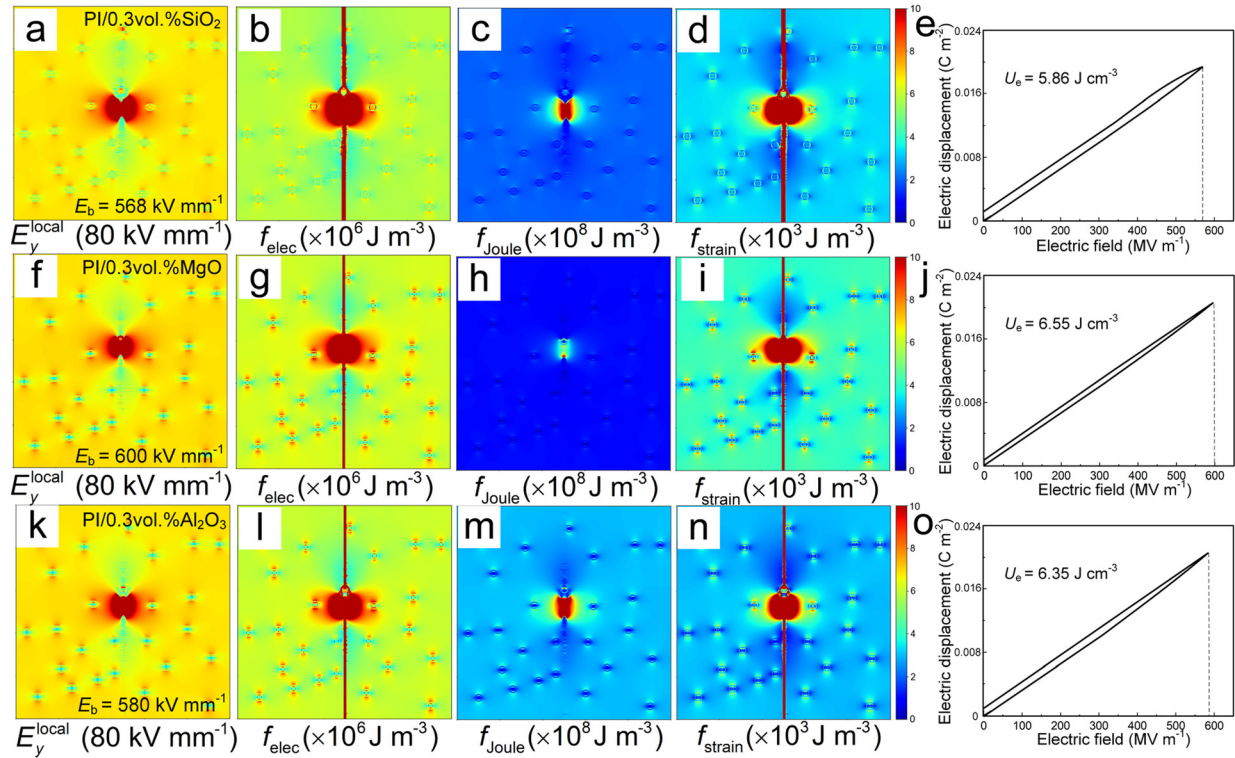


FIG. 4. Electrical field distribution, electric energy density f_{elec} , Joule heat energy density f_{Joule} , strain energy density f_{strain} , and calculated D - E loop of nanocomposites with different nanofillers. (a)–(e) PI/0.3 vol.% SiO_2 (5 nm), (f)–(j) PI/0.3 vol.% MgO (5 nm), and (k)–(o) PI/0.3 vol.% Al_2O_3 (5 nm), respectively.

dielectric constant in the PI matrix is independent of the nanofiller type. As shown in Figs. 4(c), 4(h), and 4(m), the Joule energy density distribution of PI/0.3 vol.% SiO_2 , PI/0.3 vol.% MgO, and PI/0.3 vol.% Al_2O_3 , respectively. The f_{Joule} of PI/0.3 vol.% MgO is the lowest of the three nanocomposites, indicating that the lowest electrical conductivity is obtained by doping with MgO to form the deepest electron trap. Figures 4(d), 4(i), and 4(n) show the strain energy density distribution of PI/0.3 vol.% SiO_2 , PI/0.3 vol.% MgO, and PI/0.3 vol.% Al_2O_3 nanocomposites, respectively. The PI/0.3 vol.% Al_2O_3 nanocomposites can gain the highest mechanical properties due to superior Young's modulus. The D - E loops illustrate that PI/0.3 vol.% MgO achieves the highest discharged energy density of 6.55 J cm^{-3} , followed by PI/0.3 vol.% Al_2O_3 at 6.35 J cm^{-3} and PI/0.3 vol.% SiO_2 at 5.86 J cm^{-3} , as presented in Figs. 4(e), 4(j), and 4(o), respectively. These results position PI/0.3 vol.% MgO as a promising candidate for high energy density dielectric applications, while PI/0.3 vol.% Al_2O_3 exhibits advantageous mechanical properties. This work provides valuable insights for optimizing polymer nanocomposites to improve energy storage and mechanical performance.^{17,29}

Phase-field simulations show that volume fraction, size, and type of nanofiller are key variables in determining the dielectric response and energy storage properties of polymer nanocomposites. To further explore the underlying physical mechanisms, we constructed an ensemble PINNs framework to analyze the structure-property relationships, as presented in Fig. 5(a). The PINNs framework integrates physical laws with machine learning by embedding partial differential

equations and boundary conditions into the neural network's loss function, ensuring that the model remains consistent with established physical principles while learning from the data. We construct 16 descriptors, including phase field variables, temperature, nanofiller volume fraction, material properties (dielectric constant, electrical conductivity, Young's modulus), and crucial charge transport parameters, to train the PINNs. These descriptors enable accurate modeling of charge transport behavior by Schottky injection and hopping conduction mechanisms, the dielectric response equation captures interfacial interactions between nanoparticles and the polymer matrix. Therefore, the Poisson equation was integrated to model electric field-induced polarization and charge distribution in the nanocomposites. The core of the PINNs framework is integrating the physical equations of phase-field models directly into the neural network architecture. By embedding these governing equations into the network's loss function, the PINN can maintain physical fidelity while learning from limited simulation data, significantly enhancing the model's predictive accuracy and generalizability.

The PINNs were trained using a dataset including dielectric constant, electric field distribution, breakdown strength, and electric, thermal, and strain energy densities generated from phase field simulations. By incorporating these datasets, the PINNs can learn the microstructural evolution of composites through embedded physical constraints and predict the energy storage and breakdown behavior. The 500 phase field simulation results are divided into 80% for training and 20% for testing. In the training process, k -fold cross-validation

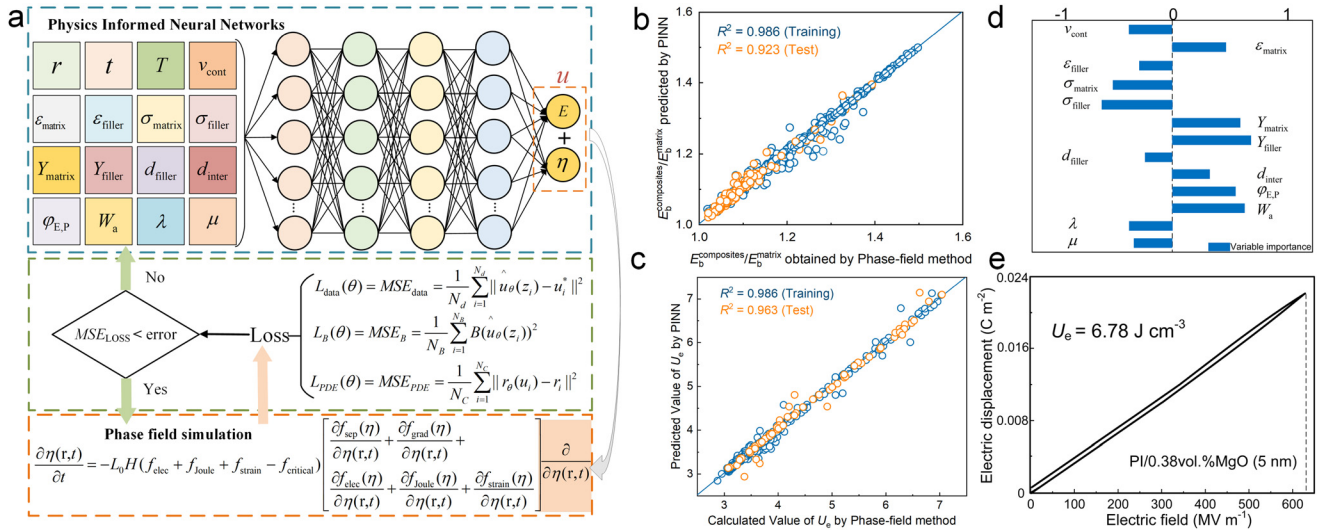


FIG. 5. Framework of the PINNs workflow. (a) The process of PINNs model for phase-field simulation. (b) Comparisons of breakdown strengths between the phase-field model and the PINNs' prediction. (c) Comparisons of energy densities between the phase-field model and the PINNs' prediction. (d) The variable importance of descriptor in determining energy storage performance. (e) The $D-E$ loop of PI/0.38 vol.% MgO nanocomposites.

($k=5$) was introduced to enlarge the size of the training set. The results show high accuracy in predicting both breakdown strength ($R^2 = 0.986$ for training and $R^2 = 0.923$ for testing) and energy density ($R^2 = 0.986$ for training and $R^2 = 0.963$ for testing), with predictions closely matching the phase field simulation results, as illustrated in Figs. 5(b) and 5(c), respectively. We employ the dropout layers to assess feature importance, revealing that ϵ_{matrix} , Y_{matrix} , Y_{filler} , d_{inter} , $\phi_{\text{E,P}}$, and W_a have a positive impact and that v_{cont} , ϵ_{filler} , σ_{matrix} , σ_{filler} , d_{filler} , λ , and μ have a negative impact on the energy storage performance, as shown in Fig. 5(d). The results indicate introducing nanofillers with low dielectric constant, low electrical conductivity, and high Young's modulus can effectively improve the breakdown strength of nanocomposites.^{28,31,32} Furthermore, doping with a small volume fraction of nanofillers with a dielectric constant similar to the polymer matrix can significantly improve the dielectric constants of nanocomposites through nanostructure engineering. The $D-E$ loops for the PI/0.38 vol.% MgO nanocomposites demonstrate a linear dielectric response with minimal hysteresis, achieving an energy density of 6.78 J cm^{-3} , indicating efficient energy storage, as shown in Fig. 5(e). The PINNs framework provides a robust tool for modeling and optimizing material behavior by combining data with physical constraints, offering valuable insights for the design of high-performance nanocomposites.

This paper presents a conduction model that combines Richardson-Schottky (RS) emission with hopping conduction to describe charge injection and transport in polymer nanocomposites. We utilize phase-field simulations incorporating electrical-thermal-mechanical breakdown mechanisms to investigate the effects of nanofiller volume fraction, size, and dielectric constant on dielectric response and breakdown behavior. The study examines electric field distribution, phase evolution, and energy densities to elucidate the physical mechanisms underlying the dielectric response and breakdown evolution of different nanofillers. Furthermore, we propose that

Physics-Informed Neural Networks (PINNs) integrate charge transport conduction, phase evolution, and boundary conditions to predict the breakdown process in nanocomposites. PINNs framework for the phase-field method can effectively predict essential material properties, such as electric field distribution, breakdown strength, and energy densities, offering a powerful tool for designing advanced polymer nanocomposites.

See the [supplementary material](#) for additional information on simulation details.

This research was funded by the National Natural Science Foundation of China grants 52377023, 52007094 (to C.Y.), 52307178, 92166203 (to Q.L.), and 51921005 (to J.L.H.) and supported by the Hunan Youth Talents Plan (2023RC3014).

AUTHOR DECLARATIONS

Conflict of Interest

The authors have no conflicts to disclose.

Author Contributions

Dong-Duan Liu: Data curation (equal); Formal analysis (equal); Methodology (equal); Software (equal); Writing – original draft (equal). **Qiao Li:** Formal analysis (equal); Supervision (equal). **Yu-Jie Zhu:** Formal analysis (equal); Methodology (equal). **Ruo-Jie Cheng:** Methodology (equal); Supervision (equal). **Tan Zeng:** Investigation (equal); Supervision (equal). **Hongxiao Yang:** Data curation (equal); Supervision (equal). **Jun Ma:** Supervision (equal); Visualization (equal). **Jin-Liang He:** Funding acquisition (equal); Methodology (equal); Validation (equal). **Qi Li:** Funding acquisition (equal); Supervision (equal). **Chao Yuan:** Conceptualization (equal); Funding

acquisition (equal); Methodology (equal); Writing – review & editing (equal).

DATA AVAILABILITY

The data that support the findings of this study are available from the corresponding authors upon reasonable request.

REFERENCES

- ¹B. Q. Wan, X. D. Dong, X. Yang, J. Q. Wang, M. S. Zheng, Z. M. Dang, G. Chen, and J. W. Zha, *Adv. Mater.* **35**, 2301185 (2023).
- ²Q. Li, L. Chen, M. R. Gadinski, S. H. Zhang, G. Z. Zhang, H. U. Li, E. Iagodkine, A. Haque, L. Q. Chen, T. N. Jackson, and Q. Wang, *Nature* **523**, 576 (2015).
- ³X. Y. Huang, B. Sun, Y. K. Zhu, S. T. Li, and P. K. Jiang, *Prog. Mater. Sci.* **100**, 187 (2019).
- ⁴J. Chen, Y. Zhou, X. Y. Huang, C. Y. Yu, D. L. Han, A. Wang, Y. K. Zhu, K. M. Shi, Q. Kang, P. L. Li, P. K. Jiang, X. S. Qian, H. Bao, S. T. Li, G. N. Wu, X. Y. Zhu, and Q. Wang, *Nature* **615**, 62 (2023).
- ⁵Y. Zhou, S. M. Peng, J. Hu, and J. L. He, *IEEE Trans. Dielectr. Electr. Insul.* **24**, 1308 (2017).
- ⁶S. H. Wang, J. Y. Li, and S. T. Li, *IEEE Trans. Dielectr. Electr. Insul.* **29**, 62 (2022).
- ⁷C. Yuan, Y. Zhou, Y. J. Zhu, S. X. Hu, J. J. Liang, Z. Luo, B. Gao, T. Zeng, Y. R. Zhang, J. Li, S. S. Huang, Z. F. Han, X. Yang, Y. Yang, P. F. Meng, J. Hu, J. L. He, H. Yuan, and Q. Li, *ACS Sustainable Chem. Eng.* **10**, 8685 (2022).
- ⁸Q. Chen, Y. Shen, S. Zhang, and Q. Zhang, *Annu. Rev. Mater. Res.* **45**, 433 (2015).
- ⁹Y. Thakur, T. Zhang, C. Iacob, T. N. Yang, J. Bernholc, L. Q. Chen, J. Runt, and Q. M. Zhang, *Nanoscale* **9**, 10992 (2017).
- ¹⁰Q. Chen, J. W. Zha, J. W. Zhai, D. L. Zhang, X. M. Bian, G. Chen, and Z. M. Dang, *Appl. Phys. Lett.* **115**, 102904 (2019).
- ¹¹C. Yuan, D. D. Liu, Y. J. Zhu, T. Zeng, B. X. Jiang, C. X. Tang, Y. Zhou, J. L. He, and Q. Li, *Appl. Phys. Lett.* **122**, 112904 (2023).
- ¹²Z. M. Dang, J. K. Yuan, J. W. Zha, T. Zhou, S. T. Li, and G. H. Hu, *Prog. Mater. Sci.* **57**, 660 (2012).
- ¹³S. J. Ding, S. H. Yu, X. D. Zhu, S. H. Xie, R. Sun, W. H. Liao, and C. P. Wong, *Appl. Phys. Lett.* **111**, 153902 (2017).
- ¹⁴C. Yuan, Y. Zhou, Y. J. Zhu, J. J. Liang, S. J. Wang, S. M. Peng, Y. S. Li, S. Cheng, M. C. Yang, J. Hu, B. Zhang, R. Zeng, J. L. He, and Q. Li, *Nat. Commun.* **11**, 3919 (2020).
- ¹⁵Y. Zhou, Y. J. Zhu, W. H. Xu, and Q. Wang, *Adv. Energy Mater.* **13**, 2203961 (2023).
- ¹⁶L. Li, J. S. Cheng, Y. Y. Cheng, T. Han, Y. Liu, Y. Zhou, Z. B. Han, G. H. Zhao, Y. Zhao, C. X. Xiong, L. J. Dong, and Q. Wang, *J. Mater. Chem. A*, **9**, 23028 (2021).
- ¹⁷X. J. Liu, M. S. Zheng, G. G. Chen, Z. M. Dang, and J. W. Zha, *Energy Environ. Sci.* **15**, 56 (2022).
- ¹⁸L. Li, J. S. Cheng, Y. Y. Cheng, T. Han, Y. Liu, Y. Zhou, G. H. Zhao, Y. Zhao, C. X. Xiong, L. J. Dong, and Q. Wang, *Adv. Mater.* **33**, 2102392 (2021).
- ¹⁹Z. H. Shen, J. J. Wang, J. Y. Jiang, Y. H. Lin, C. W. Nan, L. Q. Chen, and Y. Shen, *Adv. Energy Mater.* **8**, 1800509 (2018).
- ²⁰Z. H. Shen, J. J. Wang, J. Y. Jiang, S. X. Huang, Y. H. Lin, C. W. Nan, L. Q. Chen, and Y. Shen, *Nat. Commun.* **10**, 1843 (2019).
- ²¹D. Yue, Y. Feng, X. X. Liu, J. H. Yin, W. C. Zhang, H. Guo, B. Su, and Q. Q. Lei, *Adv. Sci.* **9**, 2105773 (2022).
- ²²D. D. Liu, Q. Li, Y. J. Zhu, B. X. Jiang, T. Zeng, H. X. Yang, J. L. He, Q. Li, and C. Yuan, *J. Phys. D* **57**, 415502 (2024).
- ²³S. Cuomo, V. S. Di Cola, F. Giampaolo, G. Rozza, M. Raissi, and F. Piccialli, *J. Sci. Comput.* **92**, 88 (2022).
- ²⁴G. E. Karniadakis, I. G. Kevrekidis, L. Lu, P. Perdikaris, S. Wang, and L. Yang, *Nat. Rev. Phys.* **3**, 422 (2021).
- ²⁵L. F. Yin, X. H. Cao, and D. D. Liu, *Appl. Energy* **332**, 120527 (2023).
- ²⁶T. Zhang, X. Chen, Y. Thakur, B. Lu, Q. Y. Zhang, J. Runt, and Q. M. Zhang, *Sci. Adv.* **6**, eaax6622 (2020).
- ²⁷M. X. Zhu, J. C. Li, H. G. Song, and J. M. Chen, *IEEE Trans. Dielectr. Electr. Insul.* **27**, 336 (2020).
- ²⁸Y. Cheng, Y. Feng, Z. B. Pan, P. Wang, J. J. Liu, L. Liang, J. H. Yu, J. W. Zhai, and Q. Wang, *Energy Environ. Sci.* **16**, 5881 (2023).
- ²⁹M. H. Yang, Z. P. Wang, Y. L. Zhao, Z. R. Liu, H. Pang, and Z. M. Dang, *Adv. Mater.* **36**, 2309640 (2023).
- ³⁰M. C. Yang, S. J. Wang, J. Fu, Y. J. Zhu, J. J. Liang, S. Cheng, S. X. Hu, J. Hu, J. L. He, and Q. Li, *Adv. Mater.* **35**, 2301936 (2023).
- ³¹J. Chen and X. Y. Huang, *Sci. Bull.* **68**, 1478 (2023).
- ³²J. Chen, Z. H. Shen, Q. Kang, X. S. Qian, S. T. Li, P. K. Jiang, and X. Y. Huang, *Sci. Bull.* **67**, 609 (2022).

Supplementary Information

Physics-informed neural networks for phase field simulation in designing high energy storage performance polymer nanocomposites

Dong-Duan Liu¹, Qiao Li^{1*)}, Yu-Jie Zhu², Ruo-Jie Cheng¹, Tan Zeng¹, Hongxiao Yang¹, Jun Ma³, Jin-Liang He⁴, Qi Li⁴, Chao Yuan^{1,*)}

AFFILIATIONS

¹College of Electrical and Information Engineering, Hunan University, Changsha 410082, China

²Department of Materials Science and Engineering, University of Wisconsin-Madison, Madison, WI, 53706, USA

³School of Electrical, Electronic and Mechanical Engineering, University of Bristol, Bristol 27267, UK.

⁴State Key Laboratory of Power System, Department of Electrical Engineering, Tsinghua University, Beijing 100084, China

***)Author to whom correspondence should be addressed:**

chaoyyy@outlook.com (C. Yuan)

qiaoli@hnu.edu.cn (Q. Li)

Physics-informed neural networks for phase field simulation

The dielectric constant of the polymer nanocomposites is a crucial component for designing high-energy density composites. Introducing trace amounts of nanofillers can significantly enhance the dielectric constant of composites by increasing the interfacial polarization between the nanofillers and the polymer matrix. To analyze the dependence of the dielectric constant on the nanofiller's concentration in dielectric polymer composites, a variety of classic models have been proposed to predict the dielectric constant of polymer nanocomposites. However, these classic dielectric constant prediction models have been applied in a wide range of composite materials without considering the interaction between the components of the composites. Recent research has demonstrated the interphase region between nanofillers and polymer matrix on the electric polarization and dielectric constant of polymer nanocomposites is evident. In recent studies, multicore models and phase-field methods have been introduced to evaluate the effect of interphase regions on the dielectric properties of polymer nanocomposites. Assuming the nanofillers have the same sizes and are homogenously dispersed throughout the polymer matrix, a mathematical model has been proposed to predict the dielectric constant of the composites by considering the dielectric properties of the interfacial region between the nanofillers and the matrix. The schematic illustration of the variations in dielectric constant across the interfacial region is shown in Figure S2 (Supporting Information). The mathematical model is expressed as,

$$\varepsilon_C^\beta = K_m \varepsilon_m^\beta + K_f \varepsilon_f^\beta + K_i \varepsilon_i^\beta$$

where ε_C^β , ε_m^β , ε_f^β , and ε_i^β are the dielectric constant of composites, polymer matrix, nanofillers, and interfacial region, respectively; K_m , K_f , K_i , and β are volume fractions of the polymer matrix, nanofillers, interfacial region, and dimension factor, respectively. Inspired by the multicore model, the K_i can be calculated by,

$$K_i = K_f \left[\left(1 + \frac{2d_{\text{inter}}}{d_{\text{filler}}} \right)^3 - 1 \right] \left(1 - \left(\frac{6K_f}{\pi} \right)^3 \right)$$

where d_{inter} and d_{filler} are the thickness of the interface and the diameter of nanofillers. Considering the interfacial polarization, the spatially varying local dielectric constant around the interfacial region within the polymer matrix is presented as,

$$\varepsilon_i(r) = \varepsilon_m + (k_2 g - k_1) e^{-g}, g = (r / d_{\text{inter}})^2$$

where r is the distance away from the surface of the nanofiller; k_2 and k_1 are the characteristic parameter of interfacial region.

The charge conduction behavior in polymers is crucial for determining the electrical insulation properties of polymers at high temperatures and electric fields. Conduction loss in polymer dielectrics are primarily influenced by electrode injection and bulk phase conduction. Schottky emission occurs at the interface between the metal electrode and the dielectric, where the charge carriers in the metal electrode overcome the energy barrier and inject into the polymer dielectric at high temperature and high electric field. Hopping conduction occurs within the polymer dielectric, where trapped charge carriers are thermally activated and jump between trap sites by tunneling effects. A modified bipolar charge injection and transport model based on the Schottky injection mechanism and hopping conduction mechanism were established to investigate the charging behavior in polymer nanocomposites under high

temperatures and electric fields. A schematic illustrating the charge conduction processes, including Schottky emission and hopping conduction is presented in Figure S3 (Supporting Information). The conduction current density at the interface between the metal electrode and the dielectric polymer is presented as,

$$J_{\text{Schottky}} = A_S T_C^2 \exp\left(-\frac{\phi_{\text{e,p}}}{K_B T_C}\right) \left[\left(\frac{\sqrt{e^3 / 4\pi\epsilon_C} \sqrt{E}}{K_B T_C} \right) \right]$$

where A_S , T_C , $\phi_{\text{e,p}}$, K_B , e , E , ϵ_C represent the Richardson coefficient, the temperature, the intrinsic injection barrier between the electrode and dielectric polymer, the Boltzmann constant, the element charge, the applied electric field, and the dielectric constant of polymer nanocomposite, respectively.

Hopping conduction is a bulk process, meaning trapped charge carriers are thermally activated and jump between trapping sites by tunneling effects. The charge transport within the polymer nanocomposites is governed by,

$$J_{\text{Hopping}} = 2n_e e \lambda_e v_e \exp\left(\frac{-W_a e}{K_B T_C}\right) \sinh\left(\frac{\lambda_e E}{2K_B T_C}\right)$$

where n_e , λ_e , v_e and W_a mean the carrier concentration, the hopping distance, the escape frequency, and the activation energy in eV, respectively.

The Schottky injection mechanism and hopping conduction mechanism elucidate the charge transport behavior of the polymer nanocomposites. Considering the charge transport behavior and the effect of nanoparticles on space charge, the potential distribution is calculated by the Poisson equation,

$$-\nabla \epsilon_p \cdot \nabla \phi_p = \rho_0$$

where ϵ_p , ϕ_p , and ρ_0 mean the relative dielectric constant of composites, the electric potential, and the space charge density, respectively.

Based on the various charge conduction models and space charge distribution, the phase-field model for electrical-thermal-mechanical breakdown simulates the breakdown phase evolution in temporal and spatial domains. This work utilized phase-field simulation methods to generate a comprehensive database of the breakdown process of polymer doped with nanofillers of different volume fractions, sizes, and dielectric constants. The database contains the breakdown strength, dielectric constant, electrical distribution, electrical, thermal, and strain energy densities of polymer nanocomposites under different applied electric fields and temperatures. We introduce a continuous phase field variable $\eta(r, t)$ to describe the temporal and spatial evolution of the microstructure. The value of phase field variable $\eta(r, t) = 0$, $\eta(r, t) = 1$, and $\eta(r, t) = 0 \sim 1$ represent the unbroken phase (matrix or filler), breakdown phase, and the region of the interface between the unbroken phase and the breakdown phase. The total free energy was denoted by the synergistic effects of the phase separation energy, the interfacial energy, the electric energy, the thermal energy, and the strain energy,

$$F_{\text{total}} = \int_V [f_{\text{sep}}(\eta(r)) + f_{\text{grad}}(\eta(r)) + f_{\text{elec}}(\eta(r)) + f_{\text{Joule}}(\eta(r)) + f_{\text{strain}}(\eta(r))] dV$$

where $f_{\text{sep}}(\eta(r))$ is the phase separation energy density, $f_{\text{grad}}(\eta(r))$ means the interfacial energy density, $f_{\text{elec}}(\eta(r))$ represents the electric energy density, $f_{\text{Joule}}(\eta(r))$ denotes the thermal energy density, $f_{\text{strain}}(\eta(r))$ means the strain energy density.

The phase separation energy density, interfacial energy density, electric energy density, thermal energy density, and strain energy density are calculated by $f_{\text{sep}}(\eta(r)) = \alpha \eta^2 (1 - \eta)^2$,

$$f_{\text{grad}}(\eta(r)) = 1/2\gamma |\nabla \eta(r)|^2, \quad f_{\text{elec}}(\eta(r)) = 1/2\varepsilon_0 \varepsilon_r E^2, \quad f_{\text{Joule}}(\eta(r)) = \sigma E^2 dt, \quad \text{and}$$

$$f_{\text{strain}}(\eta(r)) = \varepsilon_r^2 E^4 / 8Y, \text{ respectively.}$$

where α is the phase separation energy barrier, γ is the gradient energy coefficient, σ is the electrical conductivity, dt means the applied electric field of the period, Y is the Young's modulus.

A modified Allen-Cahn equation is utilized to perform the breakdown phase evolution process in the polymer nanocomposites,

$$\frac{\partial \eta(r,t)}{\partial t} = -L_0 H(f_{\text{elec}} + f_{\text{Joule}} + f_{\text{strain}}) \left[\frac{\partial f_{\text{sep}}(\eta)}{\partial \eta(r,t)} + \frac{\partial f_{\text{grad}}(\eta)}{\partial \eta(r,t)} + \frac{\partial f_{\text{elec}}(\eta)}{\partial \eta(r,t)} + \frac{\partial f_{\text{Joule}}(\eta)}{\partial \eta(r,t)} + \frac{\partial f_{\text{strain}}(\eta)}{\partial \eta(r,t)} \right]$$

where L_0 means the kinetic coefficients related to the interfacial migration rate with value of $1 \text{ m}^2 / (\text{s} \cdot \text{N})$, and $H(f_{\text{elec}} + f_{\text{Joule}} + f_{\text{strain}})$ means the Heaviside unit step function with electric energy density, thermal energy density, and strain energy density, respectively.

High-throughput computing employs powerful computational resources to facilitate the expeditious processing of a large set of computational tasks by utilizing automation and parallelization. This approach integrates databases, computational simulations, and machine learning techniques to assess and enhance the characteristics of materials, thereby accelerating the development of functional materials. High-throughput computing accelerates materials design and discovery, but its high computational resource requirements, model dependency, and complex data parsing limit its development. Physics-Informed Neural Networks (PINNs) offer a novel machine learning method combining physical principles with neural networks. By incorporating known physical laws, partial differential equations, initial conditions, and boundary conditions as constraints into the loss function of neural networks, the neural network can learn from the data and make effective modeling and predictions based on known physical laws. Moreover, solving the modified Allen-Cahn equation of the phase-field method is a typical partial differential equation numerical problem. Deepening and optimizing neural networks can improve the performance of neural networks in solving complex differential equations. Therefore, PINNs provide an innovative approach to studying the complex breakdown phase evolution process within polymer nanocomposites.

The core structure of PINNs is the deep neural network (DNN). The forward propagation process of DNN layers is,

$$u^{N_L} = \theta(z^{N_L}) = \theta(W^{N_L} u^{N_L-1} + b^{N_L})_{N_L-1}$$

where u^{N_L} , $\theta(z^{N_L})$, W^{N_L} , u^{N_L-1} , and b^{N_L} are the output, nonlinear active function, weights of DNN, the predicted output of $N_L - 1$ th layer of DNN, and offsets of the N_L -th DNN layer, respectively.

In the backpropagation process of the DNN layer, the loss function was designed to calculate the loss between the training output and the real training data. The loss function of the output layer $L(\bullet)$ is expressed as,

$$L(W^{N_L}, b^{N_L}, x, y) = \frac{1}{2} \| \theta(W^{N_L} u^{N_L-1} + b^{N_L}) - y \|_2^2$$

where x , y , and $\|S\|_2^2$ are inputs, outputs of DNN layers, and the parametric number of S , respectively.

In the training process of PINN, the loss functions of PINNs include differential equation loss $L_{PDE}(\theta)$, boundary conditions loss $L_B(\theta)$, and known data loss $L_{data}(\theta)$. The loss function of PINNs $L_{PINNs}(\theta)$ is set with mean squared error (MSE),

$$L_{PINNs}(\theta) = \alpha_{PDE} L_{PDE}(\theta) + \alpha_B L_B(\theta) + \alpha_{data} L_{data}(\theta)$$

where $L_{PINNs}(\theta)$, $L_{PDE}(\theta)$, $L_B(\theta)$, and $L_{data}(\theta)$ mean the PINNs loss, the differential equation loss, boundary conditions loss, and known data loss, respectively; α_{PDE} , α_B , and α_{data} are the weight of the differential equation loss, boundary conditions loss, and known data loss, respectively; The loss function of $L_{PDE}(\theta)$, $L_B(\theta)$, and $L_{data}(\theta)$ are calculated by,,

$$L_{PDE}(\theta) = MSE_{PDE} = \frac{1}{N_C} \sum_{i=1}^{N_C} \| r_\theta(u_i) - r_i \|^2$$

$$L_{data}(\theta) = MSE_{data} = \frac{1}{N_d} \sum_{i=1}^{N_d} \| \hat{u}_\theta(z_i) - u_i^* \|^2$$

$$L_B(\theta) = MSE_B = \frac{1}{N_B} \sum_{i=1}^{N_B} B(\hat{u}_\theta(z_i))^2$$

where N_C , N_d , and N_B are the points from PDE, training database, and boundary conditions, respectively; $r_\theta(u_i)$ is the residual predicted by PINNs, r_i is the residual calculated by PDE, $\hat{u}_\theta(z_i)$ means the predicted data with vector variables z , z is the vector variables, u_i^* is the known data.

In iteratively updating processes of PINNs, the DNNs are trained iteratively to obtain an excitation function to approximate the differential equations that define the ultimate structure of DNN by minimizing the loss function of PINNs. Moreover, we employ the adaptive moment estimation algorithm to optimize the model parameters θ . The optimal DNN parameters are obtained by minimizing the loss function according to a certain learning rate during the fixed training process of the DNN. The optimal DNN structure is integrated into the PINNs through the feedback mechanism. The nonlinear active function parameter is obtained by,

$$\theta^* = \arg \min_{\theta} (\alpha_{PDE} L_{PDE}(\theta) + \alpha_B L_B(\theta) + \alpha_{data} L_{data}(\theta))$$

where θ^* is the optimal value of the nonlinear active function parameter, $\arg \min_{\theta}(\bullet)$ is the value of the variable at the point when the minimum value is reached.

The PINN model is trained using a dataset obtained from phase-field simulations. The PINNs learn the microstructural evolution of composites through embedded physical constraints and predict the energy storage and breakdown behavior under different electric and temperature fields. A dataset including dielectric constant, electric field distribution, breakdown strength, electric, thermal, and strain energy densities of phase breakdown evolution has been constructed by phase-field simulations integrated with PINNs. In the prediction process, 80% of the dataset is divided into a training set and 20%

is set as a test set. In the training set, k -fold cross-validation ($k = 5$) was introduced to enlarge the size of the training set. Then, we employ optimal PINNs to accelerate the design of advanced polymer nanocomposites with optimized performance.

Table S1 Characteristic variable parameters of polymer and nanofillers.

	Dielectric constant	Electrical conductivity (S/m)	Young's modulus (GPa)
PI	3.1	2.2×10^{-12}	2.2
Al ₂ O ₃	10	1×10^{-12}	300
MgO	9.7	5×10^{-15}	100
SiO ₂	3.9	1×10^{-13}	280
TiO ₂	48	1×10^{-10}	230
BaTiO ₃	300	1×10^{-8}	70
SrTiO ₃	200	1×10^{-9}	70

Table S2 Structure descriptors in Physics-Informed Neural Networks.

Descriptors	Parameter Definition
r	Spatial of phase field variable
t	Temporal of phase field variable
T	Temperature
v_{cont}	Volume fraction of nanofiller
$\varepsilon_{\text{matrix}}$	Dielectric constant of polymer matrix
σ_{matrix}	Electrical conductivity of polymer matrix
Y_{matrix}	Young's modulus of polymer matrix
$\varepsilon_{\text{filler}}$	Dielectric constant of nanofiller
σ_{filler}	Electrical conductivity of nanofiller
Y_{filler}	Young's modulus of nanofiller
d_{filler}	Diameter of nanofiller
d_{inter}	Thickness of the interface
$\varphi_{\text{E,P}}$	Intrinsic injection barrier between the electrode and dielectric polymer
W_{a}	Activation energy in eV
λ	Hopping distance
μ	Carrier mobility

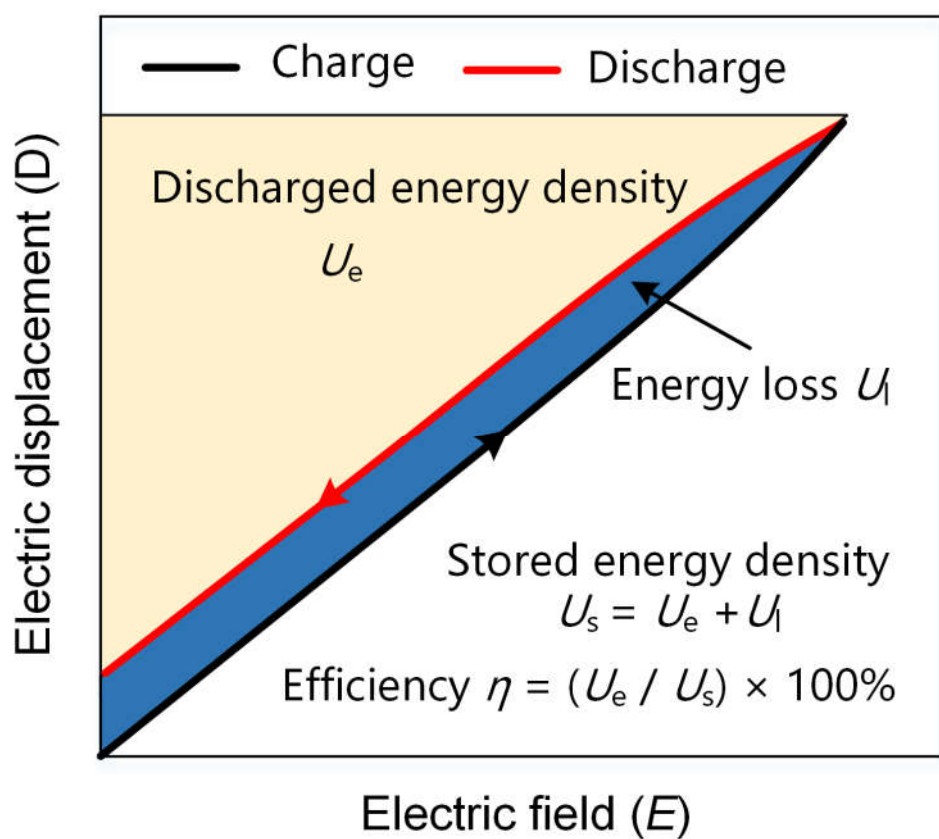


FIG. S1. Schematic diagram for calculating energy storage density and efficiency.

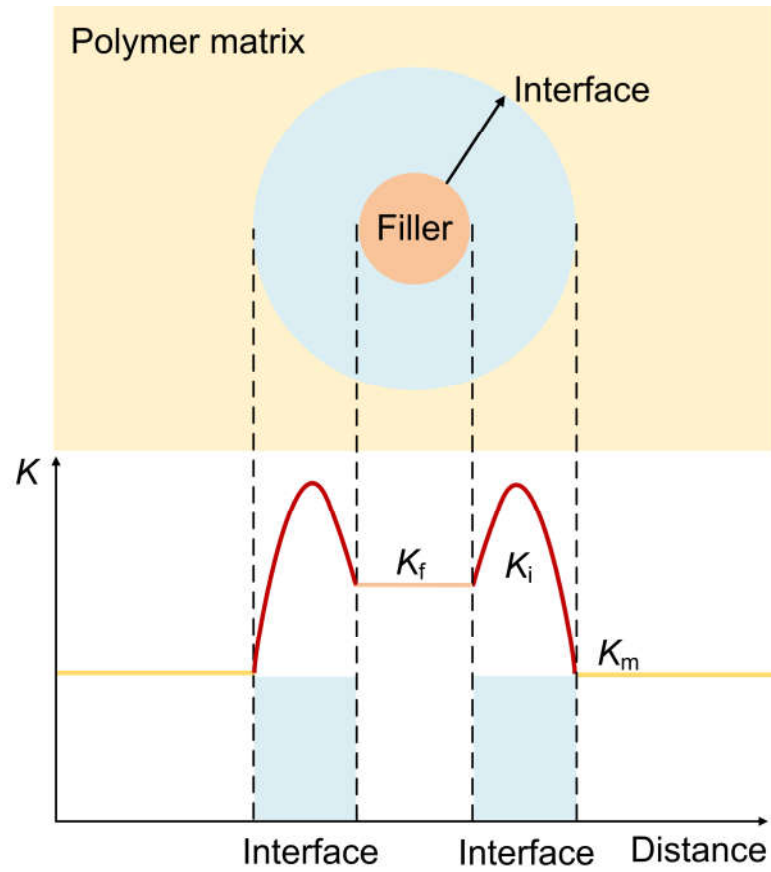


FIG. S2. Schematic illustration of the variations in dielectric constant across the interfacial region.

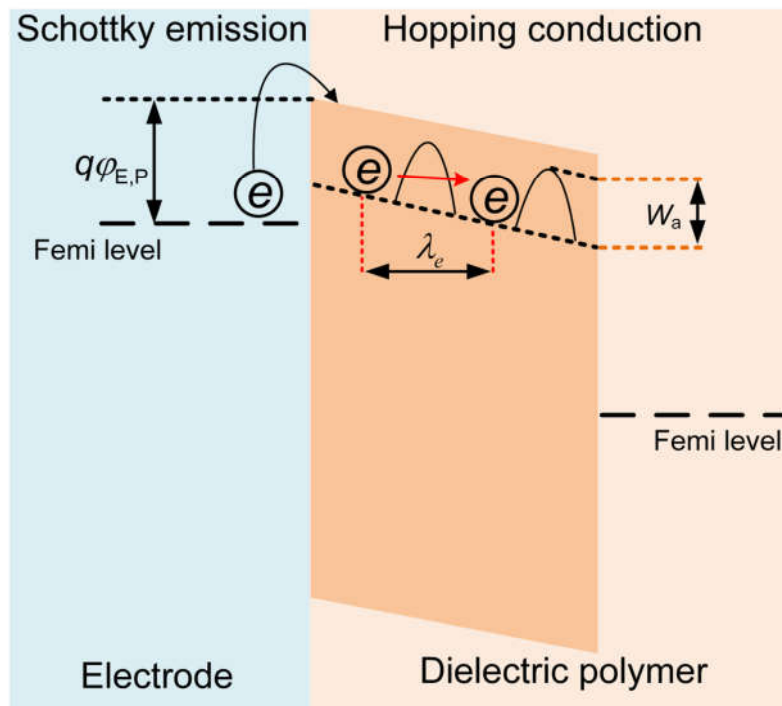


FIG. S3. Schematic of charge conduction behavior including the Schottky emission and the hopping conduction.

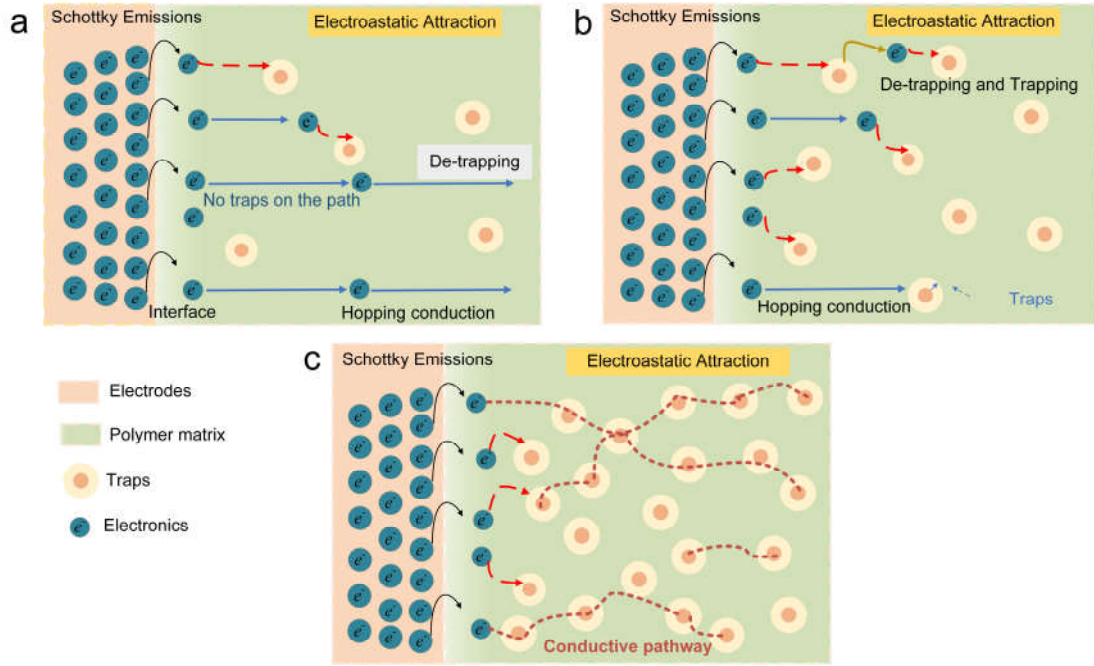


FIG. S4. Schematic of carrier movement when the trap density is (a) too sparse (0.1 vol.% nanofillers), (b) appropriate (0.3 vol.% nanofillers), and (c) too dense (1 vol.% nanofillers).

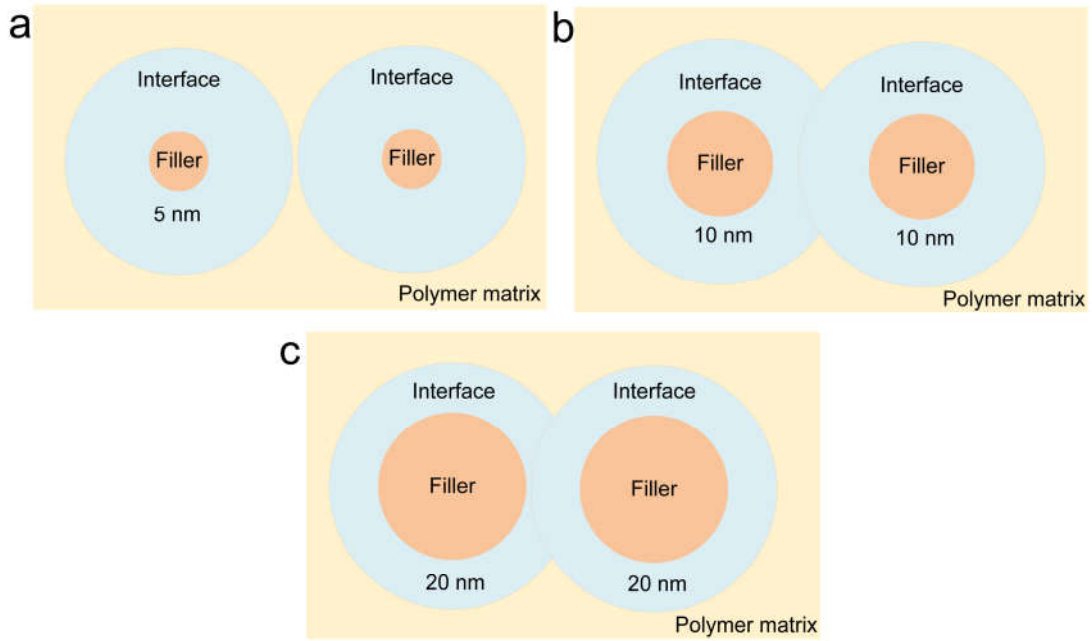


FIG. S5. Schematic distribution of fillers of different sizes and their interfaces in the polymer matrix. (a) 5 nm, (b) 10 nm, (c) 20 nm.

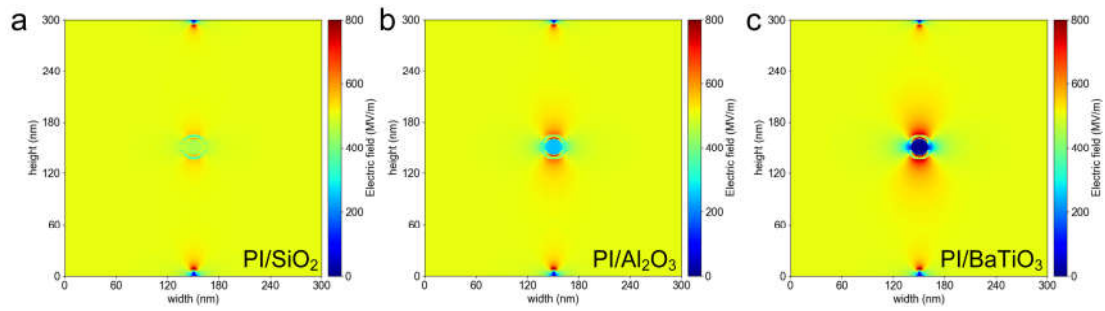


FIG. S6. Schematic representation of the electric field distortion between different nanoparticles and the polymer matrix. (a) PI/SiO₂ (3.9), (b) PI/Al₂O₃ (10), (c) PI/BaTiO₃ (300).

References

- ^{S1}Y. Thakur, T. Zhang, C. Iacob, T. N. Yang, J. Bernholc, L. Q. Chen, J. Runt, and Q. M. Zhang, *Nanoscale*. **9**, 10992 (2017).
- ^{S2}S. J. Ding, S. H. Yu, X. D. Zhu, S. H. Xie, R. Sun, W. H. Liao, C. P. Wong, *Appl. Phys. Lett.* **111**, 153902 (2017).
- ^{S3}D. Yue, Y. Feng, X. X. Liu, J. H. Yin, W. C. Zhang, H. Guo, B. Su, and Q. Q. Lei, *Adv. Sci.* **9**, 2105773 (2022).
- ^{S4}L. Li, J. S. Cheng, Y. Y. Cheng, T. Han, Y. Liu, Y. Zhou, Z. B. Han, G. H. Zhao, Y. Zhao, C. X. Xiong, L. J. Dong and Q. Wang, *J. Mater. Chem. A*. **9**, 23028 (2021).
- ^{S5}L. Li, J. S. Cheng, Y. Y. Cheng, T. Han, Y. Liu, Y. Zhou, G. H. Zhao, Y. Zhao, C. X. Xiong, L. J. Dong, and Q. Wang, *Adv. Mater.* **33**, 2102392 (2021).
- ^{S6}S. Cuomo, V. S. Di Cola, F. Giampaolo, G. Rozza, M. Raissi, F. Piccialli, *J. Sci. Comput.* **92**, 88 (2022).
- ^{S7}L. F. Yin, X. H. Cao, D. D. Liu, *Appl. Energy*. **332**, 120527 (2023).
- ^{S8}C. Yuan, Y. Zhou, Y. J. Zhu, J. J. Liang, S. J. Wang, S. M. Peng, Y. S. Li, S. Cheng, M. C. Yang, J. Hu, B. Zhang, R. Zeng, J. L. He, and Q. Li, *Nat. Commun.* **11**, 3919 (2020).
- ^{S9}L. Li, J. S. Cheng, Y. Y. Cheng, T. Han, Y. Liu, Y. Zhou, G. H. Zhao, Y. Zhao, C. X. Xiong, L. J. Dong, and Q. Wang, *Adv. Mater.* **33**, 2102392 (2021).